Fuel 136 (2014) 268–279

Contents lists available at ScienceDirect

Fuel

journal homepage: www.elsevier.com/locate/fuel

Evaluation of iron- and manganese-based mono- and mixed-metallic oxygen carriers for chemical looping combustion

Saurabh Bhavsar [a,b], Brian Tackett [a], Götz Veser [a,b,*]

[a] Chemical Engineering Department, Swanson School of Engineering, University of Pittsburgh, Pittsburgh, PA 15261, United States
[b] U.S. Department of Energy, National Energy Technology Laboratory, Pittsburgh, PA, United States

HIGHLIGHTS

- Fe_xMn_{1-x} ($x = 0...1$) bimetallic carriers were investigated for chemical looping.
- Fe-rich carriers show an unusual, reversible de-alloying/re-alloying behavior.
- Mn-rich carriers show promise due to synergistic enhancement of their redox activity.
- Use of ceria as support results in stable operation.

ARTICLE INFO

Article history:
Received 22 May 2014
Received in revised form 22 July 2014
Accepted 23 July 2014
Available online 4 August 2014

Keywords:
Chemical looping combustion
CO_2 capture
Iron
Manganese
Mixed oxides

ABSTRACT

Chemical looping combustion (CLC) is an emerging technology for clean combustion of fossil fuels with inherent CO_2 capture. In the present work, we investigate the use of iron and manganese based mixed oxides (Mn_xFe_{1-x}–CeO_2) supported on CeO_2 as oxygen carriers in CLC. The low cost and low toxicity of iron and manganese make them interesting candidates for CLC, but both mono-metallic carriers suffer from issues of low reactivity, and manganese is additionally prone to form undesired spinel structures with typical oxide supports. Mono- and bimetallic oxygen carriers were synthesized across the entire spectrum of compositions from pure Mn to pure Fe (with $x = 0$, 0.1, 0.33, 0.5, 0.8, 0.9, 1), characterized, and tested in thermogravimetric and fixed-bed reactor studies using H_2 and CH_4 as fuels. We find that the use of ceria as support results in stable operation for all compositions of the metal phase, including pure Mn. Bimetallic carriers with high Fe content, which contain a $FeMnO_3$ phase, exhibit an unusual, reversible de-alloying/re-alloying behavior during cyclic redox operation, which precludes any synergistic effects between the two metals and results in slowed reduction kinetics. However, Mn-rich carriers show a pronounced increase in carrier reactivity and selectivity for total oxidation of methane due to the addition of small amounts of Fe, indicating the promise of appropriately designed FeMn carriers as low-cost, environmentally benign oxygen carrier materials for chemical looping combustion.

1. Introduction

The development of technologies that allow for clean combustion of fossil fuels with efficient and affordable CO_2 capture is necessary to enable their continued use as a primary source of energy until cost-competitive alternate energy sources are ready for widespread deployment. Chemical looping combustion (CLC) is one of the most promising of these emerging technologies, offering a highly efficient route for clean combustion of fossil fuels with inherent CO_2 capture [1–3]. In CLC, an oxygen carrier (typically a metal oxide) is contacted with fuel in the first reactor (fuel reactor), undergoing reduction while providing necessary oxygen for the required combustion of the fuel (Fig. 1). After combustion, the reduced metal is transferred to the second reactor (air reactor) where it is re-oxidized in contact with air. The oxidized metal is then circulated back to the fuel reactor, closing the materials 'loop'. In the fuel reactor, ideally a pure mixture of CO_2 and H_2O is formed as combustion gases, from which high-concentration, sequestration ready CO_2 streams can be readily obtained via condensation of steam. Thus, CLC offers a unique and efficient route for NO_x-lean, flameless combustion of fossil fuels with inherent CO_2 capture at minimal efficiency penalty for CO_2 capture, making it rather unique among current and emerging CO_2 capture technologies [4–7].

* Corresponding author at: Chemical Engineering Department, Swanson School of Engineering, University of Pittsburgh, Pittsburgh, PA 15261, United States.
E-mail address: gveser@pitt.edu (G. Veser).

http://dx.doi.org/10.1016/j.fuel.2014.07.068
0016-2361/

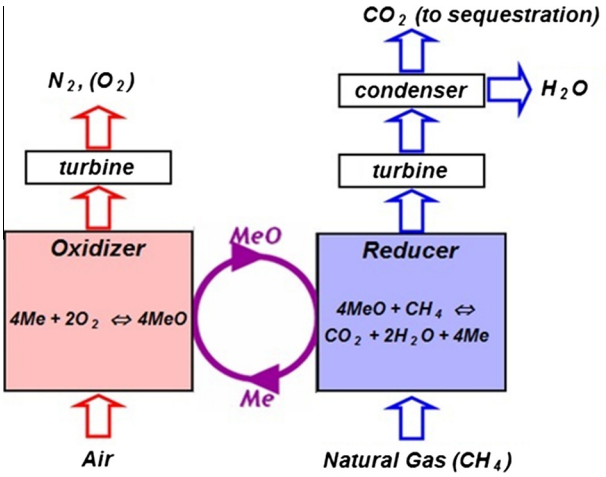

Fig. 1. Schematic for chemical looping combustion using CH_4 as fuel.

Although the concept has been demonstrated widely [8–13], there is still room for improvement in the design of efficient oxygen carriers with sufficient carrier stability and fast redox kinetics as key issues. Depending on the reactor configuration used for CLC, continuous cycling of particles between reduced and oxidized states subjects the oxygen carriers to chemical, thermal and – in transport reactor configurations – mechanical stress. Consequently, vast efforts have been made to develop efficient oxygen carriers that can cope with the harsh environment of CLC. Most of the oxygen carriers reported in the literature are synthetic carrier materials. Cu-, Ni-, Fe-, Mn-, and Co-based oxygen carriers have been investigated to evaluate their thermal stability and reactivity [14–18], with the active metal typically rendered thermally stable by supporting them on inert oxides such as Al_2O_3, SiO_2, ZrO_2, and $MgAl_2O_4$ [19–24].

Among the various metals tested for CLC, iron has recently emerged as an attractive candidate due to its low toxicity, low cost and abundance. However, its poor reactivity with typical fuels and limited oxygen transfer capacity (due to the limitation to the $Fe_2O_3 \Leftrightarrow Fe_3O_4$ transition at typical CLC operating conditions) necessitates a high solid inventory. Beyond iron, manganese constitutes another environmentally benign and low cost metal which has been identified as possible oxygen carrier. Like iron, it also exhibits multiple oxidation states that could be potentially utilized for total oxidation of fuel. However, despite this, only few studies have to-date investigated the use of Mn-based oxygen carriers, and those studies have found low reactivity and tendency to react with support oxides to form stable spinels to be limiting for the use of Mn in oxygen carriers for chemical looping [18,19,23].

We have previously shown that combining low-reactivity iron with highly active nickel through the use nickel ferrites, can improve the carrier reactivity [25]. In the present work, we are extending this approach towards investigating the effect of combining iron with manganese – a non-toxic and significantly cheaper alternative to nickel. Fe–Mn system would thus constitute low cost, environmentally benign carrier materials. Moreover, both metals naturally occur together in number of ores and minerals, making them of interest not only for engineered carrier materials but also potentially for use as natural ores.

The Fe–Mn system has been studied before, although almost exclusively in the context of so-called chemical looping oxygen uncoupling (CLOU) in which the combustion of the fuel does not occur in a direct reaction with the lattice oxygen of the carrier, but rather with gaseous oxygen that is released from the carrier at the conditions of the fuel reactor. The FeMn system promises favorable thermodynamics for gas phase oxygen release according to 6 $(Mn,Fe)_2O_3 = 4\ (Mn,Fe)_3O_4 + O_{2(g)}$ [26], as confirmed experimentally [27–29]. Among a range of Mn bimetallics tested, including Mn–Mg, Mn–Ni, Mn–Si and Mn–Fe, mixed oxides of iron and manganese were found to show good oxygen release characteristics [30,31], but in-situ X-ray studies of the phase evolution during reduction and re-oxidation of FeMn carriers indicated phase segregation during reduction [32].

In contrast to those previous studies, the present contribution is focused on the investigation of Fe–Mn carriers for "conventional" CLC applications, i.e. for conditions where lattice oxygen rather than "uncoupled" gas phase oxygen is utilized for the combustion of the fuel. Towards this purpose, we specifically synthesized Fe–Mn carriers over the entire range of Fe:Mn ratios in order to identify the impact of this ratio on the stability and activity of these carriers in CLC. However the Fe–Mn bimetallic system has been shown to undergo de-alloying during redox operation [32], and such phase segregation would eliminate any possibility of synergistic effects between the two metals. Based on our previous work which showed that the use of reducible oxides as active supports can not only strongly enhance the redox kinetics of oxygen carriers [33] but also strongly enhance phase stability of supported bimetallic nickel ferrite carriers [25], we therefore again utilize ceria as support for the Fe–Mn phases with aim of obtaining stable FeMn bimetallic carriers with improved thermal and redox stability. All carriers are synthesized by simple incipient wetness and characterized to identify the bimetallic phases formed. With this understanding, the Mn_xFe_{1-x}–CeO_2 carriers are then subjected to CLC tests using H_2 and CH_4 as fuels in a thermogravimetric analyzer (TGA) to characterize the solid phase kinetics and then further investigated in fixed-bed reactor tests to analyze gas phase (fuel) conversion and selectivity. The combination of these investigations, allows us to obtain a rather complete picture of the stability, activity, and selectivity of Fe–Mn carrier materials for CLC applications.

2. Experimental section

2.1. Oxygen carrier synthesis

Synthesis of oxygen carriers using low-cost, scalable techniques is critical in limiting the cost of oxygen carrier manufacturing. Thus, in this study oxygen carriers were synthesized in a simple and scalable two-step procedure. First the ceria support was synthesized in a hydrothermal synthesis, and Fe and Mn were deposited by incipient wetness technique.

CeO_2 was prepared by a facile hydrothermal synthesis procedure previously adapted in our research group [34] and used before for the synthesis of Ni and FeNi based oxygen carriers [25,33]. Briefly, 0.752 g of $Ce(NO_3)_3{\cdot}6H_2O$ (99 + %, Sigma–Aldrich) were dissolved in 8 ml DI water. 30 ml of NaOH (98 + %, Sigma–Aldrich) solution (7 M) was rapidly added under vigorous stirring. After 30 min of stirring, the slurry was transferred into a 50 ml autoclave, heated to 100 °C under autogenous pressure for 72 h, and then allowed to cool to room temperature. The product was washed with DI water and collected via centrifugation to remove any ionic remnants until the pH of the solution was 7. After drying the powders at 100 °C overnight and calcination at 450 °C for 2 h, the final product was obtained.

Mixed oxides of iron and manganese (Mn_xFe_{1-x}–CeO_2) with 40 wt.% FeMn weight loadings were synthesized by simple incipient wetness technique. Mn_xFe_{1-x}–CeO_2 carriers with $x = 0$, 0.1, 0.33, 0.5, 0.8, 0.9, and 1, i.e. with compositions ranging across the entire spectrum from pure Mn to pure Fe, were prepared to investigate the effect of the Fe/Mn ratio on carrier reactivity and selectivity towards total oxidation of methane. Briefly, the appropriate

amount of the respective metal nitrates ($Fe(NO_3)_3{\cdot}9H_2O$ and $Mn(NO_3)_2{\cdot}4H_2O$, both 99+%, Sigma–Aldrich) were dissolved in 1 mL ethanol (200 proof, Decon Labs, Inc.) to obtain a clear solution. 200 mg of support material was added and stirred for 2 h. The obtained slurry was dried in a vacuum oven at 80 °C overnight, and calcined at 900 °C for 2 h to obtain the final form of the oxygen carrier.

2.2. Oxygen carrier characterization

The carriers were thoroughly characterized at different stages of the experiments, i.e. after synthesis, after reactive tests in TGA, and after fixed-bed reactor tests. The specific surface area was determined via nitrogen sorption in a Micromeritics ASAP 2020 gas adsorption analyzer using the BET method. Prior to the measurement, the samples were degassed for 2 h at 200 °C under high vacuum. After calcination at 900 °C for 2 h, all the carriers had a surface area <5 m^2/g as expected due to initial sintering of carriers due to the relatively low thermal stability of ceria as support [35–38].

X-ray diffraction (XRD) measurements were performed with a powder X-ray diffractometer (Phillips PW1830) in line focus mode employing Cu Kα radiation (λ = 1.5418 Å) with typical 2θ scans between 15° and 90°. Crystal phases were identified based on JCPDS cards. Average crystal lattice spacings were determined using Bragg's law.

A JEOL JEM-2100F high-resolution transmission electron microscope (HR-TEM) was used to obtain TEM images and conduct electron energy-loss spectroscopy (EELS) to determine spatially resolved local elemental composition in the sample.

2.3. CLC reactive tests

2.3.1. Thermogravimetric analyzer (TGA) tests

Pure H_2 was used as a model fuel for initial characterization of the carrier performance during redox cycles without the added complexity of carbon formation that is associated with use of methane as fuel. Kinetics and thermal stability of the carriers with H_2 as fuel were evaluated in thermogravimetric analyzer tests (Perkin Elmer TGA-7). Subsequently, CLC redox cycles were conducted (TA instruments, SDTQ600) with CH_4 as fuel to test for carrier selectivity and thermal stability with a particular focus on carbon formation on the carrier material that would result in undesired carbon carry-over from the reducer to the oxidizer.

In a typical run, up to 15 mg of oxygen carriers were heated inside the TGA cradle in an inert gas stream (N_2 or Ar, Grade 5.0) to the desired reaction temperature of 900 °C. Then, H_2 (Grade 5.0) and air (Grade 0.1) were fed alternatingly at a flowrate of 20 sccm to simulate the periodic reduction–oxidation cycles of CLC. Between reduction and oxidation phases, the TGA was purged with N_2 or Ar (20 sccm, Grade 5.0) to avoid formation of potentially flammable gas mixtures inside the instrument. In CLC with CH_4 as fuel (Grade 2.0, 5 sccm), suitable reduction times were determined by varying the duration of the reduction half cycle and the CH_4 flowrate while monitoring the occurrence of carbon burn-off in the oxidation half cycle. All other experimental conditions were identical as above for H_2. 5–10 redox cycles were conducted in the TGA experiments in order to identify any obvious onset of deactivation of the oxygen carrier. All experiments were conducted at ambient pressure conditions.

2.3.2. Fixed-bed reactor tests

Oxygen carriers were evaluated in a fixed-bed reactor to investigate their reactivity in converting methane into steam and carbon dioxide. 100 mg of Mn_xFe_{1-x}–CeO_2 powder was placed inside the quartz-glass tubular reactor (¼″ ID), which was inserted into an electric oven (Thermo Electron Corporation – Lindberg/Blue M). A coking resistant high temperature stable thermocouple was inserted into the carrier bed to measure the actual bed temperature. The oven was heated to 900 °C, and CH_4 (1 sccm, Grade 2.0, 16.7 vol% in Ar, GHSV ~ 2274 h^{-1}) and O_2 (20 sccm, 20 vol% in He) were flown alternatingly to simulate the periodic reduction and oxidation in CLC. Depending on the reactivity of the various FeMn carriers, reduction times in FBR varied from 10 to 45 min, while the oxidation half cycle was conducted for 10 min to fully regenerate the carriers and observe complete oxygen breakthrough. In between reduction and oxidation of the carrier, the reactor was again purged with argon (Grade 5.0) to avoid formation of explosive mixtures of air and CH_4 inside the reactor. After condensation of moisture, the effluent gases were recorded using a mass spectrometer (Pfeiffer Omnistar QMS 200) and from these measurements molar flowrates (n_i) were determined for all species observed during the reaction. A carbon balance was performed at all measurements to assure the accuracy of the analysis and closed within 5–10 % error for all reported experiments.

Carbon Balance:

$$n_{CH_4,in} = n_{CH_4,out} + n_{CO_2,out} + n_{CO_{out}} + n_{\text{solid carbon}} \quad (1)$$

$$n_{CH_4,in} = n_{CH_4,out} + n_{CO_2,out} + n_{CO_{out}} + 0.5 \times (n_{H_2,out} - 2n_{CO_{out}}) \quad (2)$$

On-stream methane conversion (X_{CH4}) and cumulative carrier ($X_{carrier}$) conversion were calculated according to:

$$X_{CH_4} = \frac{n_{CH_4,in} - n_{CH_4,out}}{n_{CH_4,in}},\ X_{Carrier} = \frac{4\sum_n CO_{2,out} + \sum_n CO_{,out}}{\text{Total mol of O in carrier}} \quad (3,4)$$

Selectivity of various species (S_i) viz. CO_2, H_2, CO and carbon (C) formation by methane pyrolysis were calculated according to the following equations:

$$S_{CO_2} = \frac{n_{CO_{2,out}}}{(n_{CH_4,in} - n_{CH_4,out})},\ S_{CO} = \frac{n_{CO_{out}}}{(n_{CH_4,in} - n_{CH_4,out})} \quad (5,6)$$

$$S_{H_2} = \frac{0.5n_{H_{2,out}}}{(n_{CH_4,in} - n_{CH_4,out})}, S_{Carbon} = \frac{0.5(n_{H_{2,out}} - 2n_{CO_{out}})}{(n_{CH_4,in} - n_{CH_4,out})} \quad (7,8)$$

As expected, total oxidation, partial oxidation and catalytic pyrolysis of methane are the dominant reactions occurring in the system at all experimental conditions, which are shown below for a generic oxygen carrier, where "MeO" is metal oxide and "Me" is the reduced metal:

$$\text{Total Oxidation}: CH_4 + 4MeO \Longleftrightarrow 4Me + CO_2 + 2H_2O \quad (9)$$

$$\text{Partial Oxidation}: CH_4 + MeO \Longleftrightarrow Me + CO + 2H_2 \quad (10)$$

$$\text{Methane Pyrolysis}: CH_4(+Me) \Longleftrightarrow 2H_2 + C(+Me) \quad (11)$$

3. Results and discussion

3.1. Formation of bimetallic phases and phase stability

Understanding the structural properties of oxygen carriers is important to confidently establish structure-activity relationships. In the context of Chemical Looping Oxygen Uncoupling (CLOU), the ability to release oxygen of mixed metal oxides of iron and manganese were shown to have strong dependence on the Fe/Mn ratio. However, powder XRD results were inconclusive to determine the exact composition of monometallic and bimetallic phase [27,30]. Hence, a primary aim of the present study was the investigation of the effect of the Fe/Mn ratio on carrier phase composition, phase stability, and its impact on performance in CLC redox cycles. Therefore, all oxygen carriers were carefully characterized

to identify any bimetallic Fe–Mn phases present and their impact on the carrier reactivity in CLC redox cycles.

Mn_xFe_{1-x}–CeO_2 carriers with x = 0, 0.1, 0.33, 0.5, 0.8, 0.9, and 1, i.e. with compositions ranging across the entire range from pure Fe to pure Mn were synthesized and characterized. The phase diagram of binary Fe–Mn oxides in air is fairly well established and shows that Fe_2O_3 and Mn_2O_3 exhibit mutual solubility up to temperatures of approximately 1000 °C [26]. Depending on the Fe:Mn ratio, Fe–Mn binary systems form a spinel solid solution (Fe_3O_4–Mn_3O_4) with a 1:1 ratio of Fe and Mn, a mostly hematite containing solid solution at the Fe-rich end (Fe_2O_3 with a small amount of manganese oxide dissolved in it), and, for Mn-rich compositions, Mn_2O_3 or Mn_3O_4 rich solid solutions (depending on temperature either α-Mn_2O_3 or Mn_3O_4 with a small amount of dissolved iron oxide) [26]. Thus, the literature data confirms that iron and manganese show high affinity towards each other which can result in formation of various bimetallic phases, depending on their relative concentrations.

Fig. 2 shows the X-ray diffraction pattern of Mn_xFe_{1-x}–CeO_2 oxygen carriers subjected to calcination in air at 900 °C for 2 h. For pure Mn–CeO_2 (Fig. 2a), only peaks corresponding to Mn_2O_3 and CeO_2 are detected with no signs of the formation of a spinel phase between manganese oxide and ceria. Manganese has been reported to have a strong tendency to react with oxide supports forming spinel structures that are inactive for further redox cycles [19]. Absence of such spinels with ceria as support thus confirms the excellent suitability of ceria as support in oxygen carriers, in agreement with our previous report that ceria plays a key role in stabilizing Fe, Ni and $NiFe_2O_4$ [25,33]. Upon doping some iron into manganese oxide (Fig. 2b, c), no separate peaks of Fe_2O_3 are observed, indicating that iron is well dispersed in the Mn_2O_3 structure. With a further increase in Fe to a equimolar ratio of Mn:Fe, the bimetallic bixbyite phase ($FeMnO_3$) is observed (Fig. 2d). Fe-rich carriers (Fe:Mn > 1) shows the appearance of a Fe_2O_3 phase in addition to bixbyite (Fig. 2e). Such behavior has been observed before with ball milled samples [39]. Finally, bimetallic carriers with only 10% Mn show only diffractions corresponding to Fe_2O_3 (Fig. 2f), suggesting the absence of a bixbyite phase and the dispersion of Mn_2O_3 in the predominant hematite phase.

While information of nominal weight loadings of iron and manganese coupled with detection of the above discussed phases allows for logical peak assignment in XRD analysis, determination of relative quantities of $FeMnO_3$ (JCPDS PDF #: 76-0076) and Mn_2O_3 (JCPDS PDF #: 78-0390) is not possible, as both the bixbyite and hematite show identical diffraction patterns with almost identical relative peak intensities. Below about 300 K, α-Mn_2O_3 transforms from a cubic to an orthorhombic crystal structure [40,41], while $FeMnO_3$ exhibits cubic bixbyite phase [42]. However, despite their different crystal structures at room temperature, distinguishing between Mn_2O_3 and $FeMnO_3$ by means of lattice parameters is not possible, as they exhibit near identical values [41,42]. However, verification of the formation of the bimetallic phase is critical to understand their reactivity in redox cycles.

Therefore, $Mn_{0.5}Fe_{0.5}$–CeO_2 – i.e. a bimetallic carrier with equimolar amounts of iron and manganese – was chosen for further tests to confirm the successful formation of the bimetallic $FeMnO_3$ phase. $Mn_{0.5}Fe_{0.5}$–CeO_2 was chosen due to the ease of analysis as complete incorporation of one metal into the equimolar amount of the other would only form $FeMnO_3$ and would not result in the formation of a separate monometallic Fe_2O_3 phase. Calcination temperature variation was chosen as test parameter: As-synthesized powders were first calcined at 800 °C for X-ray analysis, and subsequently calcined at the CLC operation temperature of 900 °C. Fig. 3 shows the XRD pattern of $Mn_{0.5}Fe_{0.5}$–CeO_2 after calcination at (a) 800 °C and (b) 900 °C. It can be seen that the carrier calcined at 800 °C clearly displays the presence of free Fe_2O_3 phase in the sample, whereas the peaks corresponding to Fe_2O_3 disappear upon calcination of sample at 900 °C. Thus, absence of Fe_2O_3 diffraction peaks strongly suggests that all the iron oxide is incorporated into the cubic bixbyite structure of $FeMnO_3$, and if there is any residual free iron oxide present in the sample, it is under the detection limit of the XRD analysis.

Furthermore, TEM equipped with electron energy loss spectroscopy (EELS) was used to understand the spatial distribution of the metals at the nanometer scale. Fig. 4 shows a typical TEM and elemental maps of Mn, Fe and Ce in the $Mn_{0.5}Fe_{0.5}$–CeO_2 sample. It can be observed that iron and manganese are well dispersed in the sample, and they are found in close vicinity of each other. No separate islands of iron (i.e. devoid of manganese) could be found.

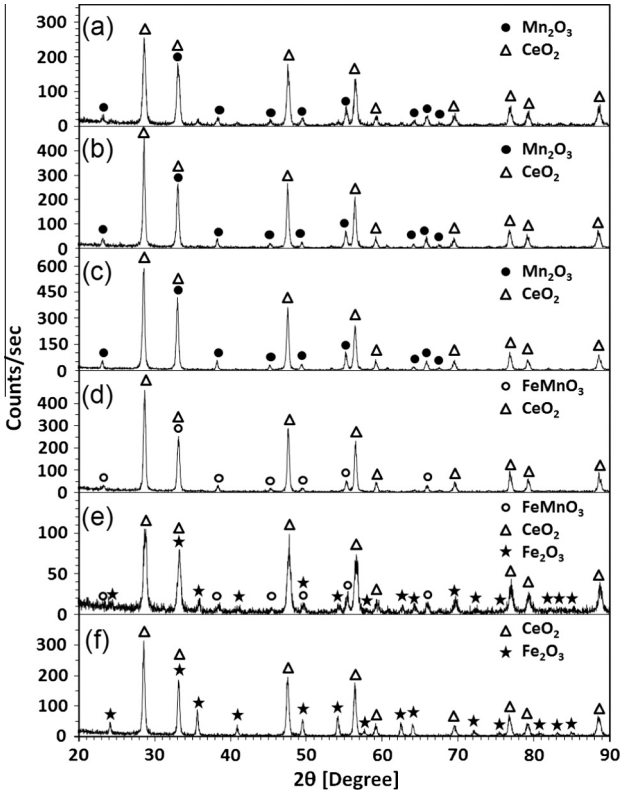

Fig. 2. Typical X-ray diffraction patterns of Mn_xFe_{1-x}–CeO_2 carriers after calcination at 900 °C for 2 h (0.2 SLM air) where (a) x = 1, (b) x = 0.9, (c) x = 0.8, (d) x = 0.5, (e) x = 0.33 and (f) x = 0.1.

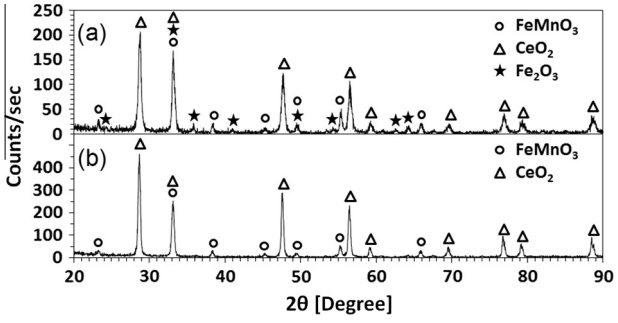

Fig. 3. X-ray diffraction pattern showing the effect of calcination temperature (a) 800 °C and (b) 900 °C on $Mn_{0.5}Fe_{0.5}$–CeO_2 (calcined in 0.2 SLM air for 2 h). Calcination of carriers at 900 °C leads to loss of free Fe_2O_3 phase confirming formation of bimetallic $FeMnO_3$ phase.

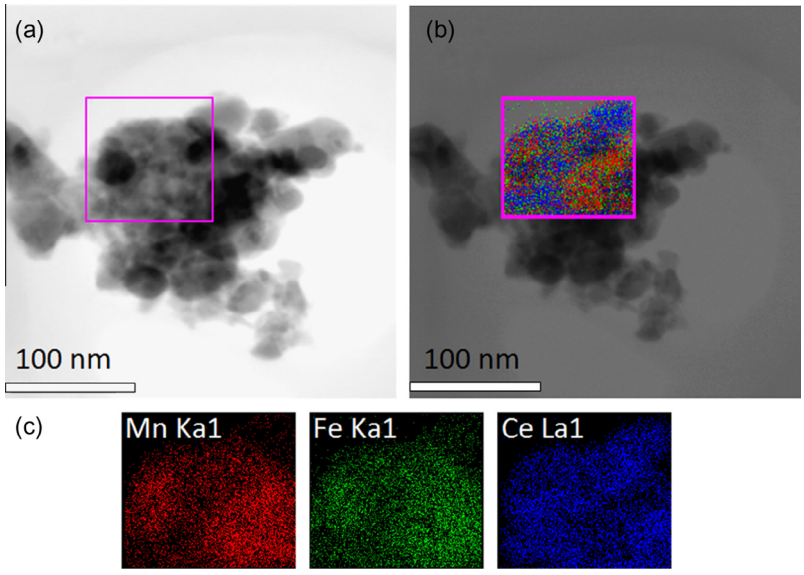

Fig. 4. TEM image of a $Mn_{0.5}Fe_{0.5}$–CeO_2 sample (a) without and (b) with superimposed EELS elemental maps; and c) elemental distribution of individual elements Mn (left), Fe (middle) and Ce (right) after calcination at 900 °C in 0.2 SLM air for 2 h (scale of the distribution maps is ~100 * 100 nm). The EELS analysis confirms occurrence of Fe and Mn in close vicinity on the nanometer scale.

Thus EELS analysis is in agreement with the formation of $FeMnO_3$ in the $Mn_{0.5}Fe_{0.5}$–CeO_2 sample.

Finally, Rietveld refinement was performed as an auxiliary test using the commercially available software PANalytical X'Pert Highscore Plus to determine quantitative phase composition of $Mn_{0.5}Fe_{0.5}$–CeO_2. The required high resolution data was obtained by powder diffraction measurements using a Brukers D8 Discover, equipped with LynxEye Detector. Rietveld analysis resulted in good fitting, and the $Mn_{0.5}Fe_{0.5}$–CeO_2 sample was found to contain 42.6% $FeMnO_3$, 0.2% Mn_2O_3, 0.4% Fe_2O_3 and 56.8% CeO_2. Therefore Rietveld analysis also re-confirms that $FeMnO_3$ is the major phase containing iron and manganese (with only minimal trace amounts of free Mn_2O_3 and Fe_2O_3). Furthermore, the metal weight loading calculated is in close agreement with the nominal weight loading of the carriers (40 wt.%).

Thus, having identified and confirmed the phase composition of the bimetallic oxygen carriers, the carriers were next subjected to CLC redox cycles to investigate their reactive properties.

3.2. Reactivity tests in TGA

As a first reactive test, all carriers were investigated using thermogravimetric analysis (TGA) via periodically exposing them to reducing (H_2 or CH_4) and oxidizing (air) environments at 900 °C in order to test carrier stability, reactivity, and oxygen carrying capacity. Higher oxidation state oxides of manganese (i.e., MnO_2 and Mn_2O_3) are known to be thermally unstable at elevated temperatures, i.e. depending on operating conditions like temperature and oxygen partial pressure they thermally decompose to a lower oxidation state under the release of gaseous oxygen [26]. As discussed in the introduction, the mechanism of this oxygen release is a key principle behind CLOU. However, this aspect has been studied in detail by the Chalmers group [27–30,43–50], and is not the focus of the present work. Instead, we avoid the complications of simultaneous gas phase and gas–solid phase combustion reactions by choosing the operation temperature of 900 °C where Mn_3O_4 is the stable oxide in equilibrium with air [26], i.e. the carriers release excess oxygen upon the first heating to operating temperature and cannot be oxidized beyond this oxidation state in subsequent redox cycles, hence avoiding any "oxygen uncoupling" activity.

In the first stage of the experiments, hydrogen was used as the model fuel to avoid complications due to undesired carbon formation. Following that, the carriers were exposed to redox cycles using methane as fuel.

3.2.1. Reactivity tests with hydrogen as fuel

All TGA tests were conducted at 900 °C with carriers being reduced in H_2 (10–30 min) and then oxidized in air (10–15 min), separated by a N_2 purge in between the two half cycles. Fig. 5 shows six redox cycles for a monometallic Mn–CeO_2 sample during cyclic operation with H_2 and air. The dotted lines in the figure depict the expected sample weight corresponding to various oxidation states of manganese (calculated based on the metal weight loading). In the experiment, the Mn_2O_3–CeO_2 carrier was first heated to the operation temperature under an inert atmosphere with 50 °C/min ramp rate. As expected and discussed above, the sample thermally decomposes during this heating phase, releasing oxygen and correspondingly losing weight, and the carrier weight eventually stabilizes at the weight corresponding to Mn_3O_4–CeO_2. Following that, the carrier shows stable periodic operation over the

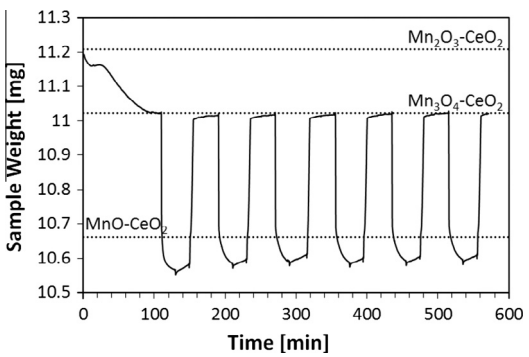

Fig. 5. Stable CLC redox cycles of Mn–CeO_2 in TGA at 900 °C with reduction in H_2, N_2 purge, and oxidation in air. The dotted lines show the calculated sample weight for various oxidation states of manganese (based on the nominal weight loading of Mn).

duration of the experiment, as indicated by virtually identical carrier weight in the reduced and oxidized states over all cycles and further confirmed in a direct comparison of the rates of weight change during the 1st and 6th oxidation and reduction half cycles shown in Fig. 6. Furthermore, the carrier shows high reactivity with a rapid loss/gain of weight in reducing/oxidizing environment. The reduction of Mn_3O_4 is restricted to MnO (confirmed via XRD, not shown here), which can also be deduced from the proximity of the expected and actual sample weight in the post-reduction purge phase. We speculate that the slight additional loss of weight can be explained by some reduction of ceria, as observed in our previous experiments [25,33]. Re-oxidation is rapid and is limited to the Mn_3O_4 oxidation state at this temperature which is in agreement with thermodynamic predictions. Thus, Mn–CeO_2 shuttles between $Mn_3O_4 \Leftrightarrow$ MnO during redox cycling with hydrogen/air at 900 °C. Compared to manganese, the contribution of ceria to the oxygen carrying capacity is limited, but the use of ceria as support allows for stable operation of supported manganese carriers. Moreover, the stable weight of oxygen carrier in the purge phase preceding reduction indicates that Mn_3O_4 decomposition does not occur at 900 °C, thus eliminating any complexity due to CLOU-related activity in our experiments. Similarly, other Mn_xFe_{1-x}–CeO_2 carriers that were tested for 5–10 cycles in CLC under the same operating conditions and showed similar stable operation (not shown here).

Compared to Mn–CeO_2, the redox cycling of the mixed oxides is more interesting to explore due to presence of the bimetallic $FeMnO_3$ phase. This is illustrated here again using the equimolar bimetallic carrier: The last redox cycle in cyclic operation of $Mn_{0.5}Fe_{0.5}$–CeO_2 is shown in Fig. 7, where dotted lines again represent the expected sample weights in various oxidation states of the carrier. The materials characterization (Section 3.1) had shown that $Mn_{0.5}Fe_{0.5}$–CeO_2 is formed upon calcination at 900 °C (Fig. 2d). However, similar to the monometallic Mn carrier, the bimetallic carrier shows thermal decomposition to the lower $Fe_3Mn_3O_8$ oxidation state during the initial heating phase, and the subsequent redox cycles do not exceed this oxidation state.

Reduction of the $Mn_{0.5}Fe_{0.5}$–CeO_2 from the $Fe_3Mn_3O_8$ oxidation state is two-staged. In the initial stage, exposure to hydrogen results in very rapid reduction in weight, and the subsequent slower reduction stage is preceded by a distinct break in the reduction profile. The carrier weight corresponding to this break is in close agreement with reduction of the carrier to a physical mixture (i.e. de-alloyed phase) of FeO and MnO or possibly an alloy of the kind (Mn,Fe)O. Furthermore, the sample weight during the post-reduction purge correlates well with a mix of (MnO + Fe)–CeO_2, which was further confirmed via XRD (Fig. 8a). Thus, the bimetallic carrier undergoes de-alloying during the reduction process and

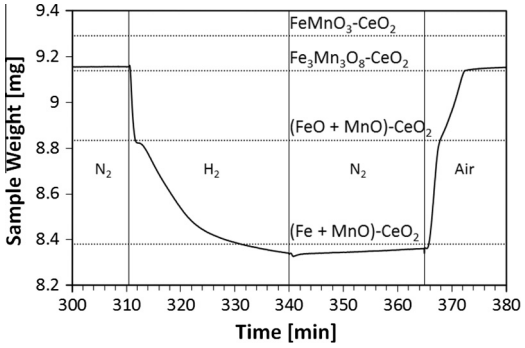

Fig. 7. Single redox cycle of $Mn_{0.5}Fe_{0.5}$–CeO_2 in TGA at 900 °C with reduction in H_2, N_2 purge, and oxidation in air. The dotted lines show the calculated sample weight for various oxidation states of manganese and iron (based on nominal weight loadings of Fe and Mn).

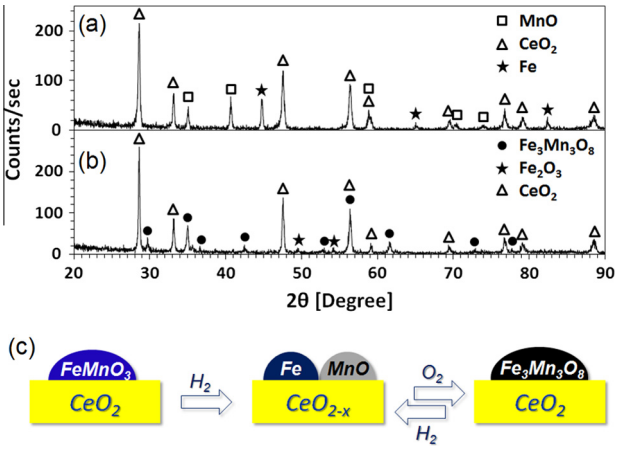

Fig. 8. X-ray diffraction pattern of $Mn_{0.5}Fe_{0.5}$–CeO_2 after (a) reduction in H_2 (20 sccm) and (b) re-oxidation in air (20 sccm) at 900 °C and (c) schematic illustration of the unusual de-alloying and re-alloying of iron and manganese observed during redox cycling of $Mn_{0.5}Fe_{0.5}$–CeO_2 in CLC at 900 °C.

phase-segregated iron oxide is reduced all the way to metallic Fe, while the reduction of manganese oxide is still restricted to MnO in the presence of iron.

Similarly, re-oxidation of the de-alloyed carrier consists of two steps with different rates of oxidation. Once again, the sample weight corresponding to the transition point between the two processes is in good agreement with the break observed in the reduction profile and thus with a (FeO + MnO) phase. Remarkably, upon

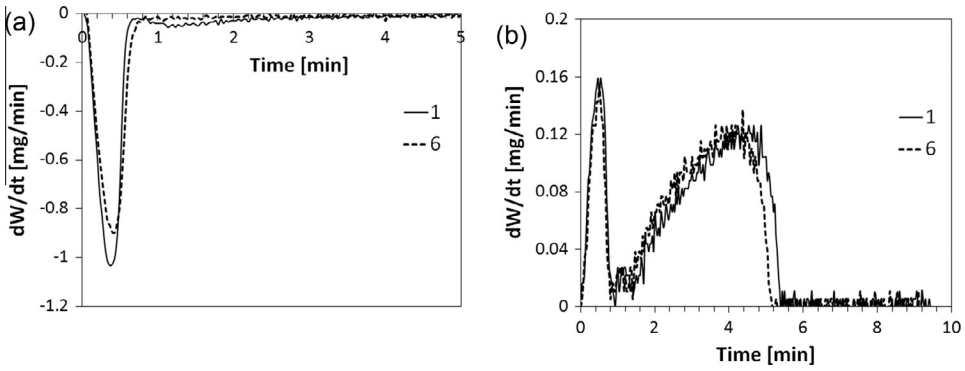

Fig. 6. Comparison of rate of weight change between first and sixth redox cycle for Mn–CeO_2 carriers during (a) reduction and (b) oxidation half cycles in TGA at 900 °C using H_2 and air respectively.

re-oxidation, the metals undergo re-alloying, re-forming the initial $Fe_3Mn_3O_8$ phase as confirmed in XRD (Fig. 8b). Absence of any Fe_2O_3 peaks in the X-ray diffraction pattern suggests that the phase-segregated iron is completely incorporated into the manganese structure. Furthermore, similar to the re-oxidation of manganese, which results in formation of Mn_3O_4 (rather than Mn_2O_3), iron associated with manganese is also restricted to the $Fe^{2+/3+}$ oxidation state.

Unlike in the equimolar $Mn_{0.5}Fe_{0.5}$–CeO_2 carrier, the more iron-enriched $Mn_{0.33}Fe_{0.67}$–CeO_2 carrier shows the presence of free iron which undergoes full oxidation to Fe_2O_3, resulting in a mix of $Fe_3Mn_3O_8$ and Fe_2O_3 (not shown here).

Thus, these Mn_xFe_{1-x}–CeO_2 carriers exhibit an unusual de-alloying and re-alloying behavior, schematically summarized in Fig. 8c. Although use of ceria stabilizes supported manganese by avoiding the formation of a spinel phase, it cannot alter the thermodynamics of iron and manganese oxides and maintain the integrity of the bimetallic phase during redox operation. Such atypical large-scale migration of metals when exposed to redox environment has been reported before, where reduction of the bixbyite phase resulted in formation of a (Mn,Fe)O alloy phase which subsequently bleed metallic iron [32]. Table 1 summarizes the various iron and manganese phases detected by XRD at different stages of redox cycling, i.e. post-calcination, post-reduction and post-reoxidation, for all the carriers in the present study.

For very Fe-rich carriers, calcined $Mn_{0.1}Fe_{0.9}$–CeO_2 only shows the presence of Fe_2O_3 and no separate Mn-oxide diffractions are observed in XRD (Fig. 2f). These carriers were also subjected to redox cycling in H_2-TGA, and XRD of the reduced sample confirms the presence of metallic Fe along-with weak reflections of MnO (Table 1). Thus, the sample shows some signs of de-alloying, and after subsequent re-oxidation of the carrier only Fe_2O_3 could be detected. In combination with the material balance in TGA, this observation suggests that for very Fe-rich carriers, Mn is able to freely bleed in-and-out of the Fe-oxide structure depending on the reducing or oxidizing environment.

Finally, on the other end of the composition spectrum, Mn-rich carriers ($Mn_{0.9}Fe_{0.1}$–CeO_2 and $Mn_{0.8}Fe_{0.2}$–CeO_2) show the presence of only Mn_2O_3 after calcination. Surprisingly, carriers removed from redox cycling in the reduced state confirm formation of MnO with minor traces of metallic iron in XRD (Table 1). This suggests that most of the iron is still dispersed in the MnO structure, i.e. that the Mn-rich carriers do not undergo phase separation. Re-oxidation of the carriers forms Mn_3O_4 and shows no signs of a free iron oxide phase.

For a direct comparison of the behavior of all carriers in these H_2/air redox cycles, Fig. 9a summarizes the oxygen carrier utilization and reduction kinetics as a function of composition [i.e. Fe-content = $n_{Fe}/(n_{Fe} + n_{Mn})$]. Here, carrier utilization is defined as the ratio of oxygen consumed to total oxygen contained in the carrier. Thus, for pure iron or manganese carriers, shuttling between $Fe_2O_3 \Leftrightarrow Fe$ and $Mn_2O_3 \Leftrightarrow Mn$, respectively, would result in carrier utilization of 1. The straight, solid line in Fig. 9a represents the carrier utilization obtained for a pure linear superposition of the oxygen carrying capacity of a pure Mn and a pure Fe-based carrier (i.e. for a simple physical mixture of iron and manganese carriers); the line does not take into account any additional oxygen that might be supplied by a reducible support like ceria. Since manganese only shuttles between $Mn_3O_4 \Leftrightarrow MnO$ and thus only partially utilizes the theoretically available lattice oxygen, it results in a rather low carrier utilization of 0.22, as indicated by this line for Fe = 0%. For pure Fe, carrier utilization is 1, since iron can undergo complete redox cycling between $Fe_2O_3 \Leftrightarrow Fe$. Hence, going across from pure Mn to pure Fe, the carrier utilization represented by the line increases monotonously with increasing iron content.

In the same graph, the rate of reduction is represented by the rate of loss of oxygen $(dn_o/dt)_{avg}$ (in moles, averaged over the range of 0–80% of relative carrier utilization), normalized by weight of the oxygen carrier [W_{ox}] in the oxidized state. Since the rate of oxygen loss slows down substantially towards the end of the reduction half-cycle due to exhaustion of active material, the rate of loss of oxygen was averaged only over the range of 0–80% oxygen consumption.

From Fig. 9a, it can be seen that carrier utilization obtained during redox cycling of Mn–CeO_2 is in agreement with a cycling between $Mn_3O_4 \Leftrightarrow MnO$. Similarly, as expected, Fe–CeO_2 shows complete carrier utilization. The slight increase in the carrier utilization compared to the expected theoretical values can again be attributed to a small contribution from reduction of the ceria support, as reported before [25,33]. For all bimetallic Mn_xFe_{1-x}–CeO_2 carriers, the carrier utilization is in close agreement with the values predicted from a linear superposition of the pure components. This makes sense in view of the above discussed evidence for de-alloying of iron and manganese during the reduction half cycle in TGA, which results in the formation of free MnO and Fe (see also Table 1). Although the two phases re-alloy during subsequent re-oxidation, such large-scale de-alloying eliminates the possibility of synergistic effects by combining iron and manganese with the aim of altering the thermodynamic properties of the resulting carriers.

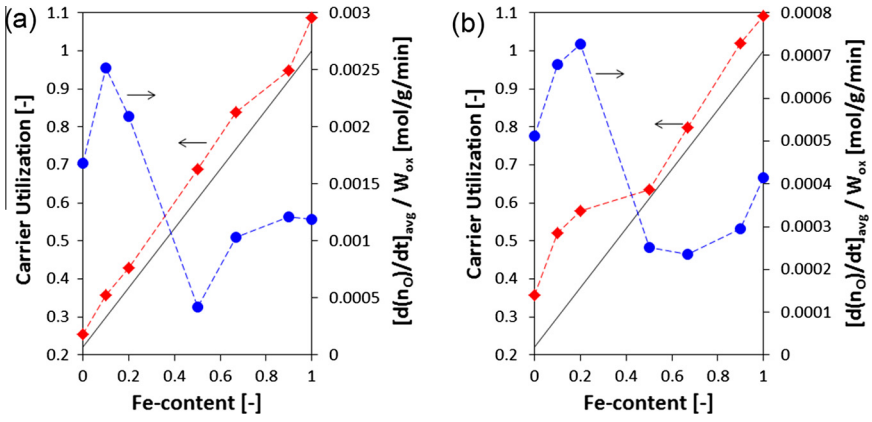

Fig. 9. Carrier utilization and rate of oxygen loss ($d(n_o)/dt_{,avg}$; averaged over 0–80% oxygen utilization and normalized by the weight of the oxidized carrier, W_{ox}) for Mn_xFe_{1-x}–CeO_2 carriers as a function of Fe-content in TGA redox cycles at 900 °C using (a) H_2 and (b) CH_4 as fuel. The gray solid line corresponds to the calculated carrier utilization for a linear superposition of the monometallic carriers (i.e. a physical mixture of Fe- and Mn-oxides).

Table 1
Iron and manganese phases detected in XRD for Mn_xFe_{1-x}–CeO_2 carriers subjected to calcination and redox cycling at 900 °C. Phases in parenthesis are minor phases in the sample with only one or two low-intensity diffraction peaks detectable in the XRD spectrum.

Carriers	Phases detected in XRD		
	After calcination	After redox cycling in TGA at 900 °C	
		Reduced (H_2 or CH_4)	Re-oxidized (air)
Mn–CeO_2	Mn_2O_3	MnO	Mn_3O_4
$Mn_{0.9}Fe_{0.1}$–CeO_2	Mn_2O_3	MnO, (Fe)	Mn_3O_4
$Mn_{0.8}Fe_{0.2}$–CeO_2	Mn_2O_3	MnO, (Fe)	Mn_3O_4
$Mn_{0.5}Fe_{0.5}$–CeO_2	$FeMnO_3$	MnO, Fe	$Fe_3Mn_3O_8$
$Mn_{0.33}Fe_{0.67}$–CeO_2	$FeMnO_3$, Fe_2O_3	MnO, Fe	$Fe_3Mn_3O_8$, Fe_2O_3
$Mn_{0.1}Fe_{0.9}$–CeO_2	Fe_2O_3	MnO, Fe	Fe_2O_3
Fe–CeO_2	Fe_2O_3	Fe	Fe_2O_3

While pure manganese has a lower effective oxygen carrying capacity than iron, the rate data in Fig. 9a shows that it has a significantly higher rate of reduction. Additionally, doping small quantities of iron into manganese further increases the rate of oxygen consumption. As discussed above, iron is completely dissolved into the Mn_2O_3 structure in these carriers and these results hence suggest that the presence of this dopant might change the oxygen activity in this oxide, making it more facile to react with the fuel.

In contrast to that, carriers with $FeMnO_3$ as the major phase show reduced rates of oxygen loss. This can be understood by the de-alloying of the carriers, as the drastic drop in reduction kinetics concurs with the occurrence of FeO + MnO (or a mixed phase of (Mn,Fe)O; see Fig. 7), and subsequent reduction is quite slow (and slower than that of pure iron oxide). This agrees with a previous report that reduction of (Mn,Fe)O is slow and consists of gradual bleed-out of iron atoms which form large iron particles, which were large enough to be detected by XRD [32]. Thus the strong drop in the average reduction rate can be attributed to the large-scale migration of iron, i.e. the solid state diffusion of Fe is becoming the slow, rate-limiting step in the reduction. On the other end of the composition spectrum, for Fe-rich carriers, doping of manganese shows only marginal effects.

Overall, the cyclic TGA tests with hydrogen as fuel show that in-situ de-alloying of iron and manganese hampers any possible synergy between the two metals in these carriers. On the contrary, the large-scale migration of iron results in slowed reduction rates. Surprisingly, doping manganese with iron results in accelerated redox kinetics. As a next step, we look to validate these results by employing methane as fuel for CLC tests in TGA. Using this more realistic fuel, the aim is to investigate carrier resistance against coking, selectivity of the fuel oxidation for combustion products, and potential differences in redox performance as a function of carrier composition.

3.2.2. Reactivity tests with CH_4 as fuel

The objective of these experiments was to test the carrier performance with methane (as the main component of natural gas) while avoiding carbon deposition on the reduced carriers. Carbon formation and subsequent carry-over into the oxidation half cycle is not only undesirable from a process point-of-view, but also complicates the evaluation of the TGA experiments due to concomitant weight increase in the reduction half cycle. Thus, initial cycles were conducted to determine the maximum possible reduction time that can be used without significant coking the carriers. All carriers were then tested in 5–10 redox cycles and showed stable operation (not shown here).

Overall, the results obtained with methane as fuel closely match those with H_2 in TGA, and are shown only in their summary in Fig. 9b. Once again we observe that Fe–CeO_2 utilizes the full theoretical oxygen capacity, while Mn–CeO_2 shows much low carrier utilization. Fe-rich carriers and carriers with $FeMnO_3$ as a major phase show again the tendency to de-alloy during the reduction half cycle and the carrier utilization is hence again in close proximity to the "Fe–Mn linear superposition line".

Independent of the type of fuel used, Mn–CeO_2 shows a higher rate of reduction compared to Fe–CeO_2, confirming the relatively high reactivity of manganese supported on ceria. Due to the de-alloying of the $FeMnO_3$ containing carriers, the average rate of reduction decreases again for these carriers with respect to both monometallic carriers—which can again be attributed to the slow phase separation/reduction of (Mn,Fe)O oxide—and the slight differences in trends between the curves for H_2 and CH_4 as fuel are likely due to the differences in reactivity of the carriers with these two fuels.

Similarly, for Mn-rich carriers, we see again an increase in the rate of reduction with CH_4 similar to that observed with H_2 as fuel. Since we do not observe a distinct phase of metallic Fe, most of the iron is likely still in the Mn-oxide structure during the redox cycle, and thus accelerates the oxygen release. Interestingly, unlike in the TGA tests with H_2, Mn–CeO_2 and Mn-rich carriers show a clear increase in the oxygen carrying capacity when redox cycles are fueled with methane. This observation is counter-intuitive, as methane is significantly less reactive than hydrogen. Moreover, the oxygen carrying capacity (or carrier utilization) increases for these Mn-rich carriers with increasing amount of iron. Interestingly, Mn-rich oxygen carriers were also found to show higher activity and oxygen release capacity in CLOU tests [27].

The unexpected increase in the carrier utilization for these carriers cannot be explained by a deeper reduction of ceria or complete reduction of iron within the manganese structure alone and was hence investigated further. Fig. 10a shows a single cycle in detail for a $Mn_{0.8}Fe_{0.2}$–CeO_2 carrier using CH_4 as fuel at 900 °C. Upon exposure to the reducing environment the sample rapidly loses weight, forming the intermediate (Mn,Fe)O phase or mix of FeO and MnO. Further reduction to MnO and Fe does not show a distinct break in the weight curve, and the carrier loses much more weight than estimated (with reduction rates significantly higher than those of bulk ceria, the reduction of which is very slow [33]). Moreover, the reduced sample shows no distinct Fe phase (only a single very low intensity peak is observed, see Fig. 10b), which indicates that iron is still present in the MnO structure. EELS analysis (not shown here) also failed to detect any phase segregated iron particles or islands, with iron found only concomitant with manganese, supporting the interpretation of the XRD results. Thus, one can hypothesize that during reduction of the (Mn,Fe)O phase, Fe^{2+} occupying the Mn^{2+} sites in the fcc structure might be undergoing reduction to form Fe^0 centers. Formation of such species would create vacancies in the oxygen lattice of the MnO structure, possibly making it more facile to reduce. However, we only observe the MnO phase in XRD (Fig. 10b), no metallic manganese phase is detected. Nevertheless, detection of such an unstable phase (e.g. MnO_{1-y}) is difficult as it might undergo oxidation with

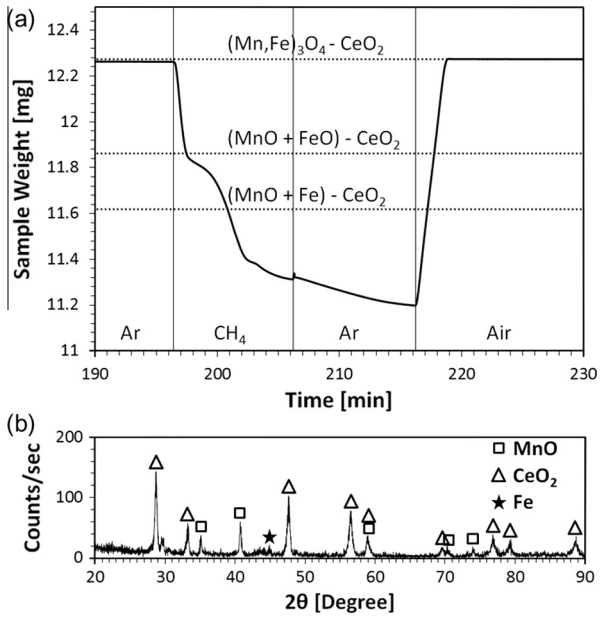

Fig. 10. (a) Single redox cycle of $Mn_{0.8}Fe_{0.2}$–CeO_2 in TGA at 900 °C using CH_4 as fuel (5 sccm), argon purge (20 sccm) and air oxidation (20 sccm) and (b) XRD of $Mn_{0.8}Fe_{0.2}$–CeO_2 carrier after reduction in TGA using CH_4 at 900 °C.

ambient air during sample transfer from TGA to XRD, and, in the absence of in-situ XRD characterization (which was not available for the present studies) the attribution of the enhanced reducibility to a deeper reduction of the Mn in the bimetallic phase remains speculative.

Overall, the use of Mn_xFe_{1-x}–CeO_2 oxides with a bixbyite or hematite phase do not show any synergistic effect due to the de-alloying of the carriers during the reduction half cycle. On the other hand, surprisingly, Mn-rich oxides containing small amounts of iron are found to be much more reactive than pure manganese.

3.3. Reactive tests in fixed-bed reactor

While TGA tests provide important insights into carrier reactivity, oxygen carrying capacity and stability of the oxygen carrier materials, the flow configuration (and hence gas–solid contacting pattern) in a TGA is not representative for the conditions in fixed-bed or fluidized bed reactors. Therefore, TGA tests cannot yield any insight into fuel conversion or product selectivity in the gas phase. However, selectivity for total combustion of the fuel is a critical parameter in comparing the efficacy of oxygen carrier in the CLC process, as CLC aims to maximize carbon capture via complete combustion of fuel to CO_2 and steam. Side reactions, such as partial oxidation and pyrolysis/cracking of the fuel, are undesired. Thus, as a last step in the present investigation, Mn_xFe_{1-x}–CeO_2 carriers were subjected to redox operation in a fixed-bed reactor configuration.

In a typical experiment, the oxygen carrier bed was brought to the reaction temperature of 900 °C under inert gas and then methane (16.7 vol% in Ar) was flown over the (initially oxidized) carriers. Moisture was condensed from the product stream in a steam trap and the product gases were then analyzed by mass-spectrometry. Reduction was continued until the carriers were fully reduced, easily monitored by a selectivity switch from total to partial oxidation and finally to methane cracking on the reduced metals. The reduction half cycle was terminated once methane cracking was detected in order to avoid formation of excess carbon on the reduced carriers. The reactor was then purged in Ar and the carriers were re-oxidized in a stream of 20 vol% O_2 in He. During the oxidation, evolution of CO and CO_2 was monitored as an indication for carbon burn-off. Oxygen break-through indicated complete regeneration of the carriers.

Results from these periodic fixed-bed experiments are not shown in detail here. Instead, Fig. 11 summarizes the performance of select Mn_xFe_{1-x}–CeO_2 carriers during the reduction half-cycle with methane in the fixed-bed reactor experiments with regard to the methane conversion rate (Fig. 11a), CO_2 selectivity (Fig. 11b), and rate of oxygen consumption in the carrier (Fig. 11c) as functions of relative carrier reduction (in percent). For simplicity, the highest oxidation states of the two metals, i.e. Fe_2O_3 and Mn_2O_3, is used as the fully oxidized reference state of the carrier and the metallic state is used as the reduced reference state. Hence, only the curves for pure Fe and the Fe-rich $Mn_{0.1}Fe_{0.9}$ carriers start at 0% reduction, i.e. at their fully oxidized states, while more Mn-rich carriers can only be oxidized to the Mn_3O_4/Fe_3O_4 states (see our XRD and TGA results discussed above), resulting in a 11.1% loss of oxygen carrying capacity (i.e. the

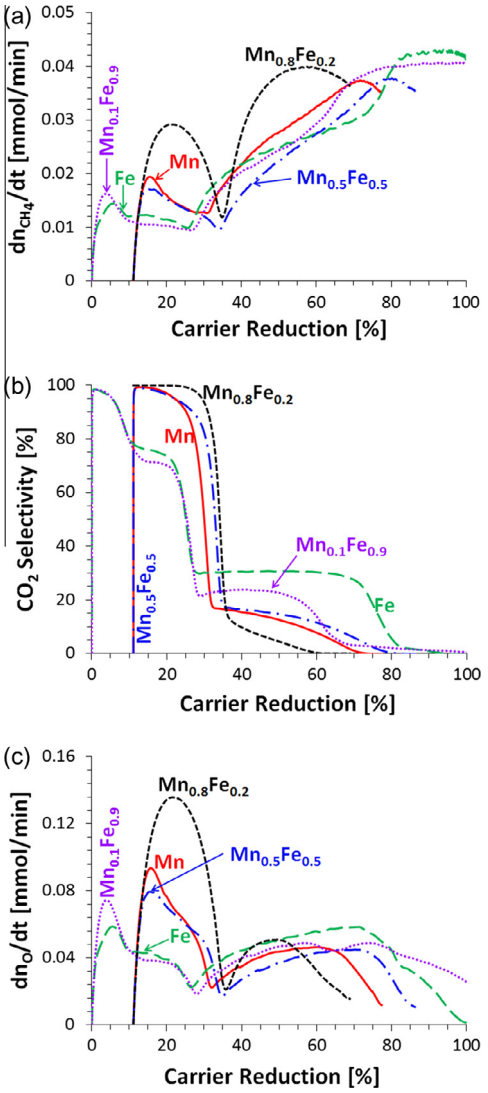

Fig. 11. Comparison of select Mn_xFe_{1-x}–CeO_2 carriers (x = 0: solid line; 0.1: dotted line; 0.5: dot-dashed line; 0.8: short-dashed line; 1: long-dashed line) during reduction with methane (16.7 vol%, 1 sccm) in fixed-bed reactor experiments at 900 °C: (a) rate of methane conversion, (b) CO_2 selectivity and (c) rate of oxygen consumption vs relative carrier reduction (in percent).

$Mn_2O_3 \Leftrightarrow Mn_3O_4$ transition) and the carrier reduction hence starts at 11.1%.

In the following discussion, we will use this data to (i) compare the monometallic Fe– and Mn–CeO_2 carriers, then (ii) evaluate the impact of Mn on Fe-based carriers by comparing monometallic iron and the $Mn_{0.1}Fe_{0.9}$–CeO_2 carrier, (iii) evaluate the impact of Fe on Mn-carriers by comparing monometallic manganese and the $Mn_{0.8}Fe_{0.2}$–CeO_2 carrier, and finally (iv) to compare the performance of the bixbyite phase ($Mn_{0.5}Fe_{0.5}$–CeO_2) with pure Mn–CeO_2.

For pure Mn–CeO_2, the initial reduction of the carrier from Mn_3O_4 to MnO is highly selective for total oxidation (see Fig. 11b) and, in agreement with the high stoichiometric demand for oxygen for this reaction path, also shows a relatively high rate of oxygen consumption from the carrier compared to further reduction of the carrier (see Fig. 11c). Under the reducing environment of methane, reduction of Mn-oxide below MnO is observed, which can be seen from Fig. 11 where the conversion, selectivity, and yield traces extend to carrier reductions well beyond 33.3% (which corresponds to MnO). Both the observations are in good agreement with TGA studies. In comparison to the monometallic Fe–CeO_2 carrier, monometallic Mn–CeO_2 shows high CO_2 selectivity during reduction of Mn_3O_4 to MnO (equivalent to ~22% of oxygen consumption), while Fe–CeO_2 is only selective towards total oxidation of methane during reduction from Fe_2O_3 to Fe_3O_4 (i.e. for ~11% of the available oxygen), i.e. Mn–CeO_2 not only shows higher carrier reactivity, but it also doubles the usable fraction of the oxygen carrier in comparison to Fe–CeO_2.

Comparing monometallic Fe– and bimetallic $Mn_{0.1}Fe_{0.9}$–CeO_2 carriers, it can be seen that adding small amounts of manganese into iron does not significantly affect the carrier reactivity. Both the rates of fuel conversion and of oxygen loss from the carrier show a marginal improvement for $Mn_{0.1}Fe_{0.9}$–CeO_2. Similarly, the highly selective range for total oxidation remains at ~0–11% of carrier reduction, i.e. the transition from Fe_2O_3 to Fe_3O_4, and is not affected by the addition of Mn. The Fe-rich carriers hence do not show any benefit of Mn addition for total oxidation of methane, which is the focus of the present report, albeit improved fuel consumption and reduced CO_2 selectivity during later stages of the reduction could be promising for partial oxidation of methane via chemical looping [51].

Increasing the Mn content to a Fe:Mn = 1:1 mixture, the bimetallic $Mn_{0.5}Fe_{0.5}$–CeO_2 shows reactivity that is strongly different from the Fe-rich carriers and instead closely resembles that of the monometallic Mn–CeO_2. The bixbyite phase shows virtually identical rates of fuel and carrier conversion to the Mn carrier, and a similar window for high CO_2 selectivity. In agreement with the results from the TGA experiments, we again see a slowdown of the reaction kinetics for higher degrees of reduction, where the de-alloying of the Mn- and Fe-phases appears again to be the rate limiting step. Also as observed in TGA, de-alloying of the carrier during the reduction process allows formation of metallic iron, therefore increasing the overall oxygen carrying capacity of the bixbyite carrier over that of the monometallic Mn carrier (from ~70% to ~80%).

Finally, on the Mn-rich end of the composition spectrum, a strong effect of the addition of Fe into Mn-based carriers can be seen: $Mn_{0.8}Fe_{0.2}$–CeO_2 shows a sharp increase in the reactivity of the carriers and a further improvement of the CO_2 selectivity to ~100% during the conversion of $(Mn,Fe)_3O_4$ to (Mn,Fe)O, i.e. the window of ~11% to ~33% carrier reduction. A similar increase in the carrier reactivity has been previously observed in the context of chemical looping oxygen uncoupling studies conducted in a batch-fluidized bed reactor [27,28]. As discussed in the context of our TGA results above, addition of iron into the manganese structure appears to make the release of lattice oxygen more facile, and this seems to apply both to thermal decomposition and to chemical reduction. Although the cause of this strong increase in the carrier reactivity is not fully understood at this point, it suggests a very promising direction for further development of manganese-based carriers, as an improved understanding of the root cause for this behavior would allow a rational, targeted engineering of the metal phase (as opposed to an Edisonian trial of a multitude of compositions) and thus yield carriers with improved reactivity for CLC.

Overall, both metals chosen in the present investigation (Fe and Mn) are abundant, environmentally benign, and relatively inexpensive candidates when compared to more reactive metals like nickel and copper. Among the two, as demonstrated in the present work, manganese shows higher reactivity and twice the usable oxygen carrying capacity compared to iron – currently considered to be one of the most suitable candidates for CLC. This increased oxygen carrying capacity and carrier reactivity can help reduce the solid inventory of oxygen carrier in looping reactors, a significant consideration in the most often investigated circulating fluidized bed (CFB) configuration for CLC processes. Furthermore, use of Mn–CeO_2 carriers provides an opportunity to improve the heat balance between the exothermic air reactor and the reducer reactor, which is an endothermic stage for virtually all currently investigated CLC carrier materials (with the notable exception of copper, a much more expensive and less environmentally benign metal). The following set of equations (12 – 16) show the reaction along with the respective heat of reaction at 900 °C for methane total oxidation and carrier re-oxidation with air (oxygen) for monometallic Fe- and Mn-based systems. It can be seen that use of manganese ($Mn_3O_4 \Leftrightarrow$ MnO) results in an exothermic carrier reduction reaction, which is not the case for iron ($Fe_2O_3 \Leftrightarrow Fe_3O_4$), and thus splits the heat load from the total oxidation reaction between the two half cycles. (The net heat of reaction is of course identical for both systems, as the net reaction yields in all CLC cases the conventional total oxidation of methane.) This is particularly significant for fixed-bed CLC concepts, where heat management constitutes the most critical point in process operation [52,53]. Mn-based carriers thus present an opportunity for more effective use of autothermal fixed-bed reactors in chemical looping combustion, and addition of relatively small amounts of Fe can further improve their operation without significantly affecting the heat balance.

Iron ($Fe_2O_3 \Leftrightarrow Fe_3O_4$):

$$\text{Reduction}: 12Fe_2O_3 + CH_4 = 8Fe_3O_4 + CO_2 + 2H_2O \quad \Delta H_R = +149.2\ \text{kJ/mol} \tag{12}$$

$$\text{Oxidation}: 8Fe_3O_4 + 2O_2 = 12Fe_2O_3 \quad \Delta H_R = -950.6\ \text{kJ/mol} \tag{13}$$

Manganese ($Mn_3O_4 \Leftrightarrow$ MnO):

$$\text{Reduction}: 4Mn_3O_4 + CH_4 = 12MnO + CO_2 + 2H_2O \quad \Delta H_R = -103.0\ \text{kJ/mol} \tag{14}$$

$$\text{Oxidation}: 12MnO + 2O_2 = 4Mn_3O_4 \quad \Delta H_R = -698.4\ \text{kJ/mol} \tag{15}$$

Net reaction of combustion:

$$CH_4 + 2O_2 = CO_2 + 2H_2O \quad \Delta H_R = -801.4\ \text{kJ/mol} \tag{16}$$

4. Summary

We presented a comprehensive study of mono- and bimetallic Fe- and Mn–CeO_2 oxygen carriers for chemical looping combustion. The two metals were chosen as they are among the most

earth abundant metals, and are environmentally benign and relatively inexpensive compared to more reactive and widely investigated metals such as Ni and Cu. While Fe/Mn-carriers have previously found some attention for CLOU applications [27–31,49,50], their use for "conventional" chemical looping had to-date not found much attention, and a systematic study of the impact of the formation of mixed metal phases of these two metals was entirely lacking. Extending our previous studies on bimetallic FeNi systems, which had demonstrated the possibility of significant benefits of alloys for CLC in combining the beneficial properties of the two parent metals [25], the intent of the present study was to identify similar synergistic effects for the FeMn system.

Mono- and bimetallic Fe and Mn carrier materials were synthesized using a low-cost, scalable technique using ceria as support material. The obtained carriers were evaluated with regard to their bimetallic phase stability, reactivity, oxygen carrying capacity, and cyclic redox stability using H_2 and CH_4 as fuels in TGA and fixed-bed reactor studies.

In agreement with our previous reports [25,33], the use of ceria as support results in excellent phase stability and stable redox operation of all carriers, which is particularly noteworthy for manganese which has been shown to react with the support matrix of many typical oxygen carrier supports (such as Al_2O_3, and many others), forming spinel structures that are inert in further redox cycling. For the two monometallic carriers, both TGA and fixed-bed reactor studies confirm the significantly higher reactivity and oxygen carrying capacity of Mn–CeO_2 vs Fe–CeO_2 ($Fe_2O_3 \Leftrightarrow Fe_3O_4$; ~11% vs $Mn_3O_4 \Leftrightarrow MnO$; ~22%). Thus, improved kinetics and oxygen carrying capacity coupled with low toxicity and favorable thermodynamics (exothermicity) of the reduction half process make Mn-based oxygen carriers an attractive and pragmatic alternative to iron.

For the bimetallic Mn_xFe_{1-x}–CeO_2 carriers, all carriers show stable redox operation, although carriers with a bixbyite $FeMnO_3$ phase showed large scale migration of iron and manganese resulting in de-alloying of the metal phases. Remarkably, this de-alloying during the reduction process appears to be completely reversible during re-oxidation of the carrier (indicating that the de-alloyed metals must remain in intimate contact). Nevertheless, the de-alloying resulted in an absence of synergistic effects of combining the two metals and in fact adversely affected the carrier reactivity which appears to become rate-limited by the slow solid state diffusion process underlying the de-alloying. Unlike for ceria-supported bimetallic FeNi systems [25], the persistent de-alloying/re-alloying behavior thus negates the advantage of using ceria as support for Mn_xFe_{1-x}–CeO_2 carriers with high iron content. In contrast to that, for Mn-rich carriers with low iron content ($Mn_{0.8}Fe_{0.2}$–CeO_2 and $Mn_{0.9}Fe_{0.1}$–CeO_2), a strong improvement in the carrier reactivity over Mn–CeO_2 was observed in TGA and fixed-bed studies, which – combined with further enhanced selectivity for total oxidation of the fuel and the advantageous heats of reaction of Mn-based carriers – makes these carriers of great interest for further investigation in CLC.

Overall, our results thus show that combining two relatively low-reactive metals like iron and manganese can indeed yield synergistic effects: Rather than adding a highly reactive secondary metal (like Ni or Cu), the addition of the low-cost, but low-reactivity, Fe not only augments the carrier reactivity at reduced cost, but also mitigates the environmental impact of oxygen carriers. Although our results indicate that these bimetallic oxygen carriers can yield significant improvement over monometallic ones, it is important to gain a better mechanistic understanding of the impact of the secondary metal on the redox performance of oxygen carriers in order to enable a rational tailoring of oxygen carriers. Nevertheless, the present results demonstrate that systematic engineering of the metal phase of oxygen carriers and the use of active, i.e. reducible, support materials such as ceria can yield high-performance oxygen carriers for chemical looping processes.

Acknowledgements

This technical effort was performed in support of the U.S. Department of Energy's National Energy Technology Laboratory's on-going research under the RDS contract DE-AC26-04NT41817. Furthermore, financial support by the National Science Foundation (CBET #1159853) and by the University of Pittsburgh's Mascaro Center for Sustainable Innovation is gratefully acknowledged. Finally, we would like to thank Prashant Kumta and Karan Kadakia for their help with Rietveld analysis.

References

[1] Adanez J, Abad A, Garcia-Labiano F, Gayan P, de Diego LF. Progress in chemical-looping combustion and reforming technologies. Prog Energy Combust Sci 2012;38:215–82.
[2] Moghtaderi B. Review of the recent chemical looping process developments for novel energy and fuel applications. Energy Fuels 2012;26:15–40.
[3] Hossain MM, de Lasa HI. Chemical-looping combustion (CLC) for inherent CO_2 separations-a review. Chem Eng Sci 2008;63:4433–51.
[4] Anheden M, Svedberg G. Exergy analysis of chemical-looping combustion systems. Energy Conv Manag 1998;39:1967–80.
[5] Kvamsdal HM, Jordal K, Bolland O. A quantitative comparison of gas turbine cycles with CO(2) capture. Energy 2007;32:10–24.
[6] Naqvi R, Wolf J, Bolland O. Part-load analysis of a chemical looping combustion (CLC) combined cycle with CO_2 capture. Energy 2007;32:360–70.
[7] Wolf J, Anheden M, Yan JY. Comparison of nickel- and iron-based oxygen carriers in chemical looping combustion for CO_2 capture in power generation. Fuel 2005;84:993–1006.
[8] Adanez J, Gayan P, Celaya J, de Diego LF, Garcia-Labiano F, Abad A. Chemical looping combustion in a 10 kW(th) prototype using a CuO/Al_2O_3 oxygen carrier: effect of operating conditions on methane combustion. Ind Eng Chem Res 2006;45:6075–80.
[9] Linderholm C, Mattisson T, Lyngfelt A. Long-term integrity testing of spray-dried particles in a 10-kW chemical-looping combustor using natural gas as fuel. Fuel 2009;88:2083–96.
[10] Lyngfelt A. Oxygen carriers for chemical looping combustion – 4000 h of operational experience. Oil Gas Sci Technol 2011;66:161–72.
[11] Pröll T, Mayer K, Bolhàr-Nordenkampf J, Kolbitsch P, Mattisson T, Lyngfelt A, et al. Natural minerals as oxygen carriers for chemical looping combustion in a dual circulating fluidized bed system. Energy Procedia 2009;1:27–34.
[12] Rifflart S, Hoteit A, Yazdanpanah MM, Pelletant W, Surla K. Construction and operation of a 10 kW CLC unit with circulation configuration enabling independent solid flow control. Energy Procedia 2011;4:333–40.
[13] Shen LH, Wu JH, Xiao J, Song QL, Xiao R. Chemical-looping combustion of biomass in a 10 kW(th) reactor with iron oxide as an oxygen carrier. Energy Fuels 2009;23:2498–505.
[14] Cho P, Mattisson T, Lyngfelt A. Comparison of iron-, nickel-, copper- and manganese-based oxygen carriers for chemical-looping combustion. Fuel 2004;83:1215–25.
[15] Garcia-Labiano F, Adanez J, de Diego LF, Gayan P, Abad A. Effect of pressure on the behavior of copper-, iron-, and nickel-based oxygen carriers for chemical-looping combustion. Energy Fuels 2006;20:26–33.
[16] Jerndal E, Mattisson T, Lyngfelt A. Thermal analysis of chemical-looping combustion. Chem Eng Res Des 2006;84:795–806.
[17] Mattisson T, Lyngfelt A, Cho P. The use of iron oxide as an oxygen carrier in chemical-looping combustion of methane with inherent separation of CO_2. Fuel 2001;80:1953–62.
[18] Mattisson T, Jardnas A, Lyngfelt A. Reactivity of some metal oxides supported on alumina with alternating methane and oxygen-application for chemical-looping combustion. Energy Fuels 2003;17:643–51.
[19] Adanez J, de Diego LF, Garcia-Labiano F, Gayan P, Abad A, Palacios JM. Selection of oxygen carriers for chemical-looping combustion. Energy Fuels 2004;18:371–7.
[20] Jin HG, Okamoto T, Ishida M. Development of a novel chemical-looping combustion: synthesis of a solid looping material of $NiO/NiAl_2O_4$. Ind Eng Chem Res 1999;38:126–32.
[21] Mattisson T, Johansson M, Lyngfelt A. The use of NiO as an oxygen carrier in chemical-looping combustion. Fuel 2006;85:736–47.
[22] Sedor KE, Hossain MM, de Lasa HI. Reactivity and stability of Ni/Al_2O_3 oxygen carrier for chemical-looping combustion (CLC). Chem Eng Sci 2008;63:2994–3007.
[23] Zafar Q, Mattisson T, Gevert B. Redox investigation of some oxides of transition-state metals Ni, Cu, Fe, and Mn supported on SiO_2 and $MgAl_2O_4$. Energy Fuels 2006;20:34–44.

[24] Mattisson T, Johansson M, Lyngfelt A. Multicycle reduction and oxidation of different types of iron oxide particles – application to chemical-looping combustion. Energy Fuels 2004;18:628–37.
[25] Bhavsar S, Veser G. Bimetallic Fe–Ni oxygen carriers for chemical looping combustion. Ind Eng Chem Res 2013;52:15342–52.
[26] Muan A, Somiya S. The system of iron oxide-manganese oxide in air. Am J Sci 1880;1962(260):230–40.
[27] Azimi G, Leion H, Rydén M, Mattisson T, Lyngfelt A. Investigation of different Mn–Fe oxides as oxygen carrier for chemical-looping with oxygen uncoupling (CLOU). Energy Fuels 2012;27:367–77.
[28] Azimi G, Rydén M, Leion H, Mattisson T, Lyngfelt A. (MnzFe1–z)yOx combined oxides as oxygen carrier for chemical-looping with oxygen uncoupling. AIChE J 2013;59:582–8.
[29] Azimi G, Leion H, Mattisson T, Lyngfelt A. Chemical-looping with oxygen uncoupling using combined Mn–Fe oxides, testing in batch fluidized bed. Energy Procedia 2011;4:370–7.
[30] Shulman A, Cleverstam E, Mattisson T, Lyngfelt A. Manganese/iron, manganese/nickel, and manganese/silicon oxides used in chemical-looping with oxygen uncoupling (CLOU) for combustion of methane. Energy Fuels 2009;23:5269–75.
[31] Shulman A, Cleverstam E, Mattisson T, Lyngfelt A. Chemical – looping with oxygen uncoupling using Mn/Mg-based oxygen carriers – oxygen release and reactivity with methane. Fuel 2011;90:941–50.
[32] Lambert A, Delquié C, Clémeneçon I, Comte E, Lefebvre V, Rousseau J, et al. Synthesis and characterization of bimetallic Fe/Mn oxides for chemical looping combustion. Energy Procedia 2009;1:375–81.
[33] Bhavsar S, Veser G. Reducible supports for Ni-based oxygen carriers in chemical looping combustion. Energy Fuels 2013;27:2073–84.
[34] Liang S, Veser G. Mixed lanthana/ceria nanorod-supported gold catalysts for water–gas-shift. Catal Lett 2012;142:936–45.
[35] Fornasiero P, Balducci G, Di Monte R, Kaspar J, Sergo V, Gubitosa G, et al. Modification of the redox behaviour of CeO_2 induced by structural doping with ZrO_2. J Catal 1996;164:173–83.
[36] Mamontov E, Egami T, Brezny R, Koranne M, Tyagi S. Lattice defects and oxygen storage capacity of nanocrystalline ceria and ceria–zirconia. J Phys Chem B 2000;104:11110–6.
[37] Pengpanich S, Meeyoo V, Rirksomboon T, Bunyakiat K. Catalytic oxidation of methane over CeO_2–ZrO_2 mixed oxide solid solution catalysts prepared via urea hydrolysis. Appl Catal A – Gen 2002;234:221–33.
[38] Zhu TL, Flytzani-Stephanopoulos M. Catalytic partial oxidation of methane to synthesis gas over Ni–CeO_2. Appl Catal A – Gen 2001;208:403–17.
[39] de Medeiros SN, Luciano A, Cótica LF, Santos IA, Paesano Jr A, da Cunha JBM. Structural and magnetic characterization of the ball-milled α-Fe_2O_3–Mn_2O_3 and α-Fe–Mn_2O_3 systems. J Magn Magn Mater 2004;281:227–33.
[40] Landolt H, Börnstein R. Landoldt-Börnstein numerical data and functional relationships in science and technology new series, Group III. In: Hellwege K-H, Hellwege AM, editors, vol. 1. New York: Springer-Verlag; 1975.
[41] Geller S. Structure of [alpha]-Mn_2O_3, $(Mn0.983Fe0.017)_2O_3$ and $(Mn0.37Fe0.63)_2O_3$ and relation to magnetic ordering. Acta Crystall Sect B 1971;27:821–8.
[42] Seifu D, Kebede A, Oliver FW, Hoffman E, Hammond E, Wynter C, et al. Evidence of ferrimagnetic ordering in $FeMnO_3$ produced by mechanical alloying. J Magn Magn Mater 2000;212:178–82.
[43] Arjmand M, Azad A-M, Leion H, Lyngfelt A, Mattisson T. Prospects of Al_2O_3 and $MgAl_2O_4$-supported CuO oxygen carriers in chemical-looping combustion (CLC) and chemical-looping with oxygen uncoupling (CLOU). Energy Fuels 2011;25:5493–502.
[44] Arjmand M, Keller M, Leion H, Mattisson T, Lyngfelt A. Oxygen release and oxidation rates of $MgAl_2O_4$-supported CuO oxygen carrier for chemical-looping combustion with oxygen uncoupling (CLOU). Energy Fuels 2012;26:6528–39.
[45] Leion H, Mattisson T, Lyngfelt A. Using chemical-looping with oxygen uncoupling (CLOU) for combustion of six different solid fuels. Energy Procedia 2009;1:447–53.
[46] Mattisson T, Leion H, Lyngfelt A. Chemical-looping with oxygen uncoupling using CuO/ZrO_2 with petroleum coke. Fuel 2009;88:683–90.
[47] Mattisson T, Lyngfelt A, Leion H. Chemical-looping with oxygen uncoupling for combustion of solid fuels. Int J Greenh Gas Control 2009;3:11–9.
[48] Moldenhauer P, Rydén M, Mattisson T, Lyngfelt A. Chemical-looping combustion and chemical-looping with oxygen uncoupling of kerosene with Mn- and Cu-based oxygen carriers in a circulating fluidized-bed 300 W laboratory reactor. Fuel Process Technol 2012;104:378–89.
[49] Rydén M, Lyngfelt A, Mattisson T. CaMn0.875Ti0.125O3 as oxygen carrier for chemical-looping combustion with oxygen uncoupling (CLOU)—Experiments in a continuously operating fluidized-bed reactor system. Int J Greenh Gas Control 2011;5:356–66.
[50] Rydén M, Lyngfelt A, Mattisson T. Combined manganese/iron oxides as oxygen carrier for chemical looping combustion with oxygen uncoupling (CLOU) in a circulating fluidized bed reactor system. Energy Procedia 2011;4:341–8.
[51] Bhavsar S, Najera M, Solunke R, Veser G. Chemical looping: to combustion and beyond. Catal Today 2014;228:96–105.
[52] Noorman S, Annaland MV, Kuipers H. Packed bed reactor technology for chemical-looping combustion. Ind Eng Chem Res 2007;46:4212–20.
[53] Solunke RD, Veser G. Hydrogen production via chemical looping steam reforming in a periodically operated fixed-bed reactor. Ind Eng Chem Res 2010;49:11037–44.